Materials Science and Engineering C 50 (2015) 367–378

Contents lists available at ScienceDirect

Materials Science and Engineering C

journal homepage: www.elsevier.com/locate/msec

# Surface characterizations of laser modified biomedical grade NiTi shape memory alloys

A. Pequegnat [a,b], A. Michael [a,b,*], J. Wang [a,b], K. Lian [c], Y. Zhou [a,b], M.I. Khan [c,d]

[a] Centre for Advanced Materials Joining (CAMJ), University of Waterloo, 200 University Avenue West, Waterloo, ON N2L 3G1, Canada
[b] Centre for Bioengineering and Biotechnology (CBB), University of Waterloo, 200 University Avenue West, Waterloo, ON N2L 3G1, Canada
[c] Department of Materials Science and Engineering, University of Toronto, 184 College Street, Suite 140, Toronto, ON M5S 3E4, Canada
[d] Smarter Alloys, Inc., MaRS Centre, South Tower, 101 College Street, Suite 200, Toronto, ON M5G 1L7, Canada

ARTICLE INFO

*Article history:*
Received 29 August 2014
Received in revised form 17 December 2014
Accepted 17 January 2015
Available online 28 January 2015

*Keywords:*
NiTi
Shape memory alloy (SMA)
Laser processing
Surface characterisation
Corrosion performance
Ni ion release

ABSTRACT

Laser processing of shape memory alloys (SMAs) promises to enable the multifunctional capabilities needed for medical device applications. Prior to clinical implementation, the surface characterisation of laser processed SMA is essential in order to understand any adverse biological interaction that may occur. The current study systematically investigated two Ni-49.8 at.% Ti SMA laser processed surface finishes, including as-processed and polished, while comparing them to a chemically etched parent material. Spectrographic characterisation of the surface included; X-ray photoelectron spectroscopy (XPS), auger electron spectroscopy (AES), and Raman spectroscopy. Corrosion performance and Ni ion release were also assessed using potentiodynamic cyclic polarization testing and inductively coupled plasma optical emission spectroscopy (ICP-OES), respectively. Results showed that surface defects, including increased roughness, crystallinity and presence of volatile oxide species, overshadowed any possible performance improvements from an increased Ti/Ni ratio or inclusion dissolution imparted by laser processing. However, post-laser process mechanical polishing was shown to remove these defects and restore the performance, making it comparable to chemically etched NiTi material.


## 1. Introduction

The unique shape memory effect (SME) and pseudoelastic (PE) properties of shape memory alloys (SMAs) coupled with excellent mechanical properties and biocompatibility have made them valuable engineering materials. In particular, the near equiatomic Nickel–Titanium (NiTi) based SMAs are increasingly used in a wide variety of medical applications ranging from surgical tools for minimally invasive procedures to implantable devices [1–3]. The effectiveness of existing applications has led to the widespread acceptance of NiTi SMAs for medical devices and remains a large driving force behind on-going research and development [1]. However, many of these devices have lengthy, if not permanent, deployment times. For example, orthodontic arch wires, bone reconstruction plates, and coronary and intestinal stents are deployed longer than 30 days in the human body. Hence, the biocompatibility and corrosion performance of these alloys will play a key role in the development of NiTi devices and their continued acceptance in application.

The corrosion resistance and biocompatibility of NiTi alloys are attributed to a protective Ti-oxide layer that forms on its surface. Like other medical device alloys such as, grade 5 titanium (Ti–6Al–4V) or 316 stainless steel (SS), NiTi alloys possess a passive surface oxide layer that increases the corrosion breakdown potential and can lower the release of harmful Ni ions. As shown by Wever et al. [4], NiTi alloy breakdown potential and current density identified through cyclic potentiodynamic corrosion testing typically fall between the Ti–6Al–4V and 316 SS biomaterials if properly processed. Also, NiTi alloys have been shown to exhibit Ni ion release in an electrolytic solution during the initial few days that subsequently decreases; eventually dropping below detectable limits [5,6]. The unique nature of the NiTi surface stems from the near equiatomic ratio of Ti to Ni in the alloy. Depending on the previous processing history the surface species will contain different mixtures of Ti-based surface oxides, Ni-based oxides/hydroxides, and even elemental Ni [5,6]. As a result, the corrosion performance and Ni ion release can vary quite significantly depending on the surface condition [5–7]. Different surface treatments can drastically affect biocompatibility such as, mechanical polish, electropolish, chemical passivation, and oxide building heat treatments that are commonly applied during component fabrication [6–11]. Albeit, cases of Ni ion release from medical devices have been reported during clinical implementation [12,13], highlighting the importance of, and need for, proper characterisation; especially for material processed using novel protocols.

As SMA applications requiring complex multifunctional properties are realized, laser-processing techniques are increasingly explored to

* Corresponding author at: Centre for Advanced Materials Joining (CAMJ), University of Waterloo, 200 University Avenue West, Waterloo, ON N2L 3G1, Canada.
*E-mail address:* a2michae@uwaterloo.ca (A. Michael).

http://dx.doi.org/10.1016/j.msec.2015.01.085
0928-4931/

help achieve these unique functional requirements. The ability to precisely and rapidly tune the local material properties, opposed to traditional inaccurate and slow bulk processes, makes lasers excellent candidates for SMA processing. For example technologies such as, laser induced vaporization [14–19] and local laser annealing [20], have shown great potential to revolutionize the fabrication and design of devices. In these novel laser technologies, rapid local changes in microstructure and/or chemical composition have been shown to effectively fine tune both the pseudoelastic and shape memory properties of NiTi SMAs. However, before these novel techniques can be applied to their full potential in medical applications, it is essential to understand the effects these laser processes have on the corrosion performance and biocompatibility.

Currently, only limited studies detail the corrosion performance and biocompatibility of laser processed NiTi [9,10,21–27], while even fewer attempt to thoroughly characterize its surface [9,28]. Improvements in corrosion performance immediately following laser processing have been reported in most studies, including those by Yan et al. [21,22,27], Man et al. [23], Cui et al. [28], and Villermaux et al. [26]. Furthermore, Ni and Ti ion release from laser processed NiTi specimen was also shown to remain lower than that found in drinking water, as shown by Sevilla et al. [14]. These promising results have been attributed to a combination of mechanisms, including enhanced surface condition (i.e. reduced roughness, increased oxide stability, etc.), removal of contaminants (i.e. carbon and oxide inclusions, additional phases, etc.), and changes in nickel to titanium ratio (Ni:Ti) on the surface [9,22,23,27,28]. However, insignificant proof stemming from a lack of surface analysis limits any validation of these mechanisms. This is further complicated by inconsistencies in literature. For example, a study by Chan et al. [9] on laser welded NiTi showed a reduction in corrosion performance immediately after welding; contradicting all the aforementioned studies showing improvements in the as-processed state. Hence, a better understanding and sufficient level of confidence on the mechanisms behind the corrosion properties of laser processed NiTi SMAs are required.

The aim of the present study was to investigate the corrosion performance and biocompatibility of pulsed Nd:YAG laser processed NiTi. Specific focus was directed on characterizing changes in surface characteristics and modification to the bulk material composition and microstructure. The contributions of this study aid in forming a more solid understanding of aspects surrounding the corrosion and biocompatibility performance of laser processed NiTi materials that have been inadequately addressed in literature to date.

## 2. Experimental methods

### 2.1. Sample preparation

Commercially available 0.37 mm thick by 12 mm wide SE508 NiTi strip manufactured by Nitinol Devices and Components (NDC) Inc. was used in this study. The chemical composition of this binary NiTi alloy was 55.8 wt.% (50.7 at.%) Ni and 44.2 wt.% (49.3 at.%) Ti with maximum O and C contents of 0.05 wt.% and 0.02 wt.%, respectively. Prior to any testing, the NiTi strip was ultrasonicated for 2 min, flipping halfway, in a 7.5 vol.% hydrofluoric acid (HF), 20 vol.% nitric acid ($HNO_3$), bal. water ($H_2O$) solution to remove a thick black oxide layer. This chemical etching process uniformly reduced the thickness of the strips to 0.35 mm. The chemically etched state is referred to as CE for the remainder of this study.

A LW50A Miyachi Unitek pulsed Nd:YAG laser system with a 1.06 μm wavelength, 600 μm nominal spot diameter was used for laser processing. During laser processing, the top and bottom of the strips were shielded with argon gas to avoid oxidation. A flow rate of 14.2 L/min (30 CFH) was found to be sufficient as identified by a shiny metallic appearance. The CE strip was cleaned with acetone, ethanol then finally de-ionized water prior to laser processing, removing potential contaminants.

A pulsed laser protocol was utilized having a peak power of 0.8 kW and the pulse schedule was shown in Fig. 1a. The laser spots were overlapped by 56% to ensure that the whole sample area was processed as illustrated in Fig. 1b. Each spot was pulsed five times to achieve the desired thermomechanical properties through change in microstructure and bulk material composition; similar to that discussed in a previous work [18,19]. This material state will be referred to as laser processed (LP) state for the remainder of this study.

Mechanical polishing was used to remove any effects of the differing surface topography and chemistry created from laser processing, to better characterize the bulk material. Strips were cut in 8 × 8 mm squares and progressively ground with 600, 800, 1200 coarse, and 1200 fine grit silicon carbide paper. Polishing was then performed with a 0.03 μm colloidal silica suspension and 30% hydrogen peroxide mixture (9:1 ratio) for approximately 5 min. This mechanical polishing process uniformly reduced the thickness of the strips to 0.25 mm. This state will be referred to as laser processed and polished (LP-Pol) for the remainder of this study. Extreme care was taken to use consistent grinding/polishing protocol for each individual specimen. For microstructural analysis a similar mechanical polishing procedure was used on cross-sectioned strip followed by a 15 s chemical etch in a 3 vol.% HF, 14 vol.% $HNO_3$, bal. $H_2O$ solution.

### 2.2. Material characterisation

To characterize the thermoanalytical properties of the NiTi materials, differential scanning calorimetry (DSC) analysis was conducted using a Thermal Analysis Q2000 system equipped with refrigerated cooling. DSC curves were recorded in a temperature range from −75 °C to 120 °C using a controlled heating and cooling rate of 5 °C/min. The martensite start ($M_s$), martensite finish ($M_f$), austenite start ($A_s$), and austenite finish ($A_f$) phase transformation temperatures were measured using the TA Universal Analysis software v4.5 following the ASTM F2004-05 standard.

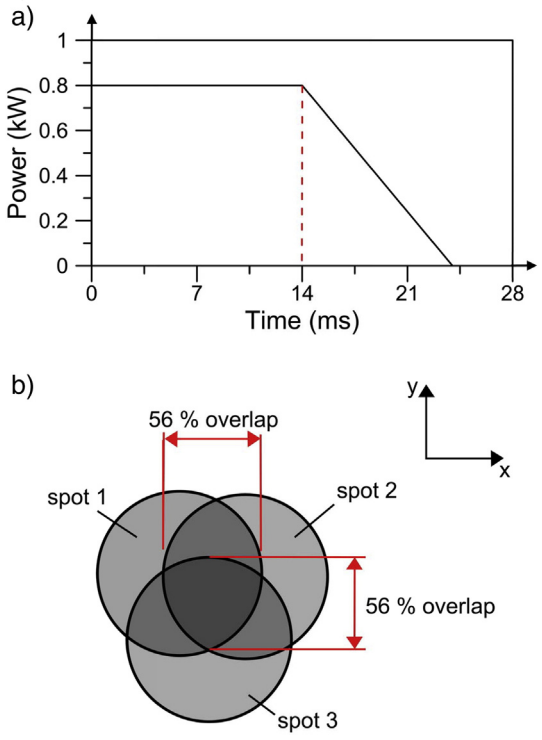


**Fig. 1.** a) Laser pulse schedule for partial penetration of NiTi strip and b) illustration of 56% overlap of laser spot configuration allowing for the complete coverage of the desired sample area.

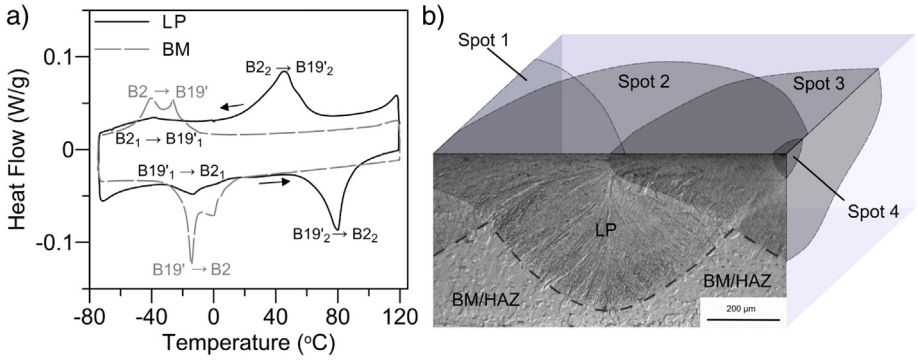


**Fig. 2.** a) Differential scanning calorimetry (DSC) results for laser processed NiTi and base material using a 5 °C heating/cooling rate and b) cross-sectional image of processed sample identifying the LP and BM/HAZ regions.

To observe the microstructure of the bulk material and the surface condition, optical microscopy (OM) was performed using an Olympus BX51M upright inspection and research microscope. The surface condition was characterized further using optical profilometry performed on a WYKO NT1100 optical profiler manufactured by Veeco having ±1 nm resolution. Three dimensional topographical surface maps of the CE, LP and LP + Pol samples and Ra roughness average values were obtained from a 1.2 × 0.92 mm area. Analysis of surface characteristics after corrosion testing was performed with the use of a JEOL JSM-6460 scanning electron microscope (SEM) with a 20 kV electron beam.

### 2.3. Surface chemistry analysis

X-ray photoelectron spectroscopy (XPS) was conducted using a K-Alpha XPS manufactured by Thermo Scientific Inc. using monochromatized Al Kα1 radiation. The source was run at 15 kV and 72 W, rastered over a 400 × 400 μm area. Sputtering was done with a 2 kV Ar+ ion beam rastered over a 2 × 2 mm area. Survey scans were taken at a pass energy of 50 eV and a binding energy range of 0–1300 eV.

Auger electron spectroscopy (AES) was performed using a PHI 660 scanning Auger microprobe. A 5 kV (~300 nA) electron beam rastered over a 100 × 100 μm area (1000×) was employed for this investigation. Sputtering was performed using a 3 kV Ar+ ion beam rastered over a 2 × 2 mm area. The sputter rate under these conditions was determined to be ~30 nm/min for a $SiO_2$ on Si layer (280 nA ion current). Sputtering rate for $SiO_2$ on Si substrate has been determined to be similar to $TiO_2$ [29]. The oxide thickness was estimated to be where the oxygen percentage dropped to half its maximum value.

Raman spectra were recorded using a Renishaw Ramanscope with a spatial resolution of $<1\ cm^{-1}$. This spectroscope was equipped with a He–Ne laser having a 633 nm wavelength and a 5 μm spot size.

### 2.4. Corrosion testing and Ni ion release measurement

Potentiodynamic corrosion tests were performed in a phosphate buffered saline (PBS) electrolyte (pH 7.4) manufactured by MP Biomedicals using a 300 mL double walled corrosion cell. The composition of the PBS electrolyte is 0.2 g KCl, 0.2 g $KH_2PO_4$, 8.0 g NaCl and 1.15 g $Na_2HPO_4$ dissolved in 1 L $H_2O$. The PBS electrolyte was used for potentiodynamic corrosion tests to maintain consistency with the Ni ion release tests. The use of PBS for corrosion testing is not uncommon [30–32], and B.G. Pound et al. [33] determined that the breakdown behaviour of NiTi in PBS is similar to Hanks' solution. A GAMRY Instruments potentiostat with Framework v4.35 software was used for controlling the tests. A three electrode configuration was used according to the ASTM F2129-08 standard for cyclic polarization testing. The reference electrode was a saturated calomel electrode (SCE) and the counter electrode was Pt mesh. The working electrode consisted of a custom sample holder, which exposed 0.25 $cm^2$ of the specimen surface area using an area limiting gasket. All tests were performed at 37 °C to simulate biological conditions. Before testing began, the solution was de-aerated with nitrogen for 30 min. The open circuit potential was measured up to 1 h, or until it was stable within 0.05 mV/s. Testing was performed at a scan rate of 0.167 mV/s, starting at −0.5 V vs SCE and increasing to 1.5 V vs SCE. Scanning was automatically reversed if the current density reached 0.1 $mA/cm^2$. A minimum of three specimens were tested for each material condition to verify reproducibility and representative curves were provided herein.

Ni ion release measurements were made using a Prodigy Inductively Coupled Plasma Optical Emission Spectroscope (ICP-OES) manufactured by Teledyne Leeman Labs Company. A Ni ion lower limit of detection (LLOD) of 13.2 μg/L (13.2 ppb) was determined during calibration. The PBS solution is commonly used for Ni ion release testing of NiTi [7,34,35]. A surface area of 1.63 $cm^2$ was immersed in 15 mL of PBS solution for 7 days ± 1 h at 37 °C. Seven days is the amount of time specified by ISO 10271 Dental Metallic Materials — Corrosion Tests and previously used by D. Vojtech et al. [36]. Moreover, it was previously found by A. Michiardi et al. [37] that Ni ion release stabilized and dropped to almost zero after 5 days. The Ni concentration in the control sample was determined to be 16.3 (±10.2) μg/L. The results provided in this work were normalized by the particular surface area for each sample and were the mean values of three measurements.

## 3. Results

In this comprehensive study the results presented below were obtained from experiments carefully designed to systematically uncover the bulk material properties of the CE, LP and LP-Pol samples, followed by their resulting surface conditions, and finally their corrosion and Ni ion release performance. First the bulk material was characterized using DSC analysis to identify the effects of laser processing on the thermoanalytical properties of the SMA as well as give insight into changes in Ti/Ni ratio. Optical microscopy was then used to understand the microstructure and identify secondary phases which may contribute to changes in the stability of the oxide layer. Next the surface characteristics of the CE, LP, and LP-Pol materials were fully characterized using optical profilometry, XPS, AES, and Raman spectroscopy to determine roughness, identify surface species present, and characterize the oxide

**Table 1**
Transformation temperatures and hysteresis (i.e. measured peak to peak) from DSC analysis.

| | $A_s$ (°C) | $A_f$ (°C) | $M_s$ (°C) | $M_f$ (°C) | Hysteresis (Δ°C) |
|---|---|---|---|---|---|
| Original BM | −20.7 | 11.1 | −15.2 | −55.7 | 30.7 |
| BM/HAZ ($B2_1 \leftrightarrow B19'_1$) | −30.7 | 2.8 | −21.6 | −55.5 | 25.4 |
| LP ($B2_2 \leftrightarrow B19'_2$) | 59.6 | 87.8 | 64.9 | 19.5 | 31.5 |

thickness and degree of crystallinity, respectively. Finally, the performance of each of the NiTi samples was assessed using cyclic potentiodynamic corrosion testing and ICP-OES for identifying Ni ions released, allowing for further discussion on the process–property–performance relationship as it applies to laser processed NiTi SMAs.

### 3.1. Thermoanalytical characterisation

From the DSC results shown in Fig. 2a it was observed that following laser processing two sets of phase transformation peaks were present. The first set of peaks observed in the LP sample, at lower temperatures, corresponds to the base material (BM) and heat affected zone (HAZ) adjacent to the laser processed material. The second set of higher temperature peaks corresponds to the Ni depleted laser processed material; as discovered in the previous work [18,19]. Fig. 2b shows the location of the LP and BM/HAZ regions in the laser processed material. As can be seen, the LP region extends well below the surface to a depth of approximately 350 μm. This relatively large depth of penetration of the laser processing is necessary to achieve the modification to the bulk composition that was observed by DSC. The phase transformation temperatures and peak to peak hysteresis are provided in Table 1. Large hysteresis between phase transformation upon heating and cooling is typical of B2 austenite ↔ B19′ martensite transformations in a binary NiTi alloy [38].

### 3.2. Microstructure

The microstructure of cross-sectioned BM (i.e. CE) and LP material is provided in Fig. 3. The BM showed an equiaxed grain structure (Fig. 3a) with many large dark etching inclusions. These inclusions are common in NiTi alloys and have previously been identified as carbon and oxygen based inclusions resulting from the ingot casting process [27]. Within the solidified laser spot epitaxial growth of grains growing from the laser spot edge toward the centre was observed (Fig. 3b and c). The aforementioned large inclusions were not present in the LP region; however, they were still detected adjacent to the laser spot in the HAZ (Fig. 3b). High temperature thermal cycles during processing induced partial recrystallization in the HAZ as shown in Fig. 3b, where fine grains were identified (Fig. 3a). At higher optical magnification, a finer secondary dark phase was observed within the LP region as shown in Fig. 3d. These phases were more prominent in the regions where multiple laser spots overlap. They result from microsegregation of Ti between dendritic grains during solidification, forming the Ti-rich $Ti_2Ni$ phase [18,19,27]. This phase is known to have limited solubility of oxygen [39]. Therefore during pulsed laser processes oxygen pick up leads to the formation of $Ti_2NiO_x$ even in Ni-rich alloys [19], since oxygen is not soluble in the NiTi matrix [39].

### 3.3. Optical microscopy and surface profiling

Surface micrographs of the CE and LP samples are shown in Fig. 4. Topographical maps are also provided in Fig. 5 for each of the sample surface conditions. The CE sample appeared to be relatively rough and with many pits. In contrast, the dendritic solidification structure of the LP material was smoother at a microscopic scale; however there are large peaks and valleys between the overlapping laser spots. Although the smoothest surface observed was from the LP-Pol sample, slight surface relief was still observed in the optical micrograph shown in Fig. 4c; likely due to thermoelastic phase transformation following mechanical grinding and polishing. The surface roughness average, Ra, was measured to be 1.63 μm, 2.43 μm and 0.01 μm for the CE, LP, and LP-Pol samples respectively (Fig. 5).

### 3.4. Surface chemistry and depth profile

A combination of XPS, AES, and Raman spectroscopy was implemented to identify the structure and chemistry of the different NiTi surfaces. First, XPS results for each of the samples are presented in Figs. 6–8. The identified species and their respective binding energies are summarized in Table 2 to aid in further discussion.

Fig. 6 shows the XPS depth profile of the CE sample. Trace amounts of elemental Ni were observed on the surface with increased intensity at longer etching times. Titanium was primarily in the form of $TiO_2$ with a shift to metallic Ti as etch depth increased. Oxygen was mostly

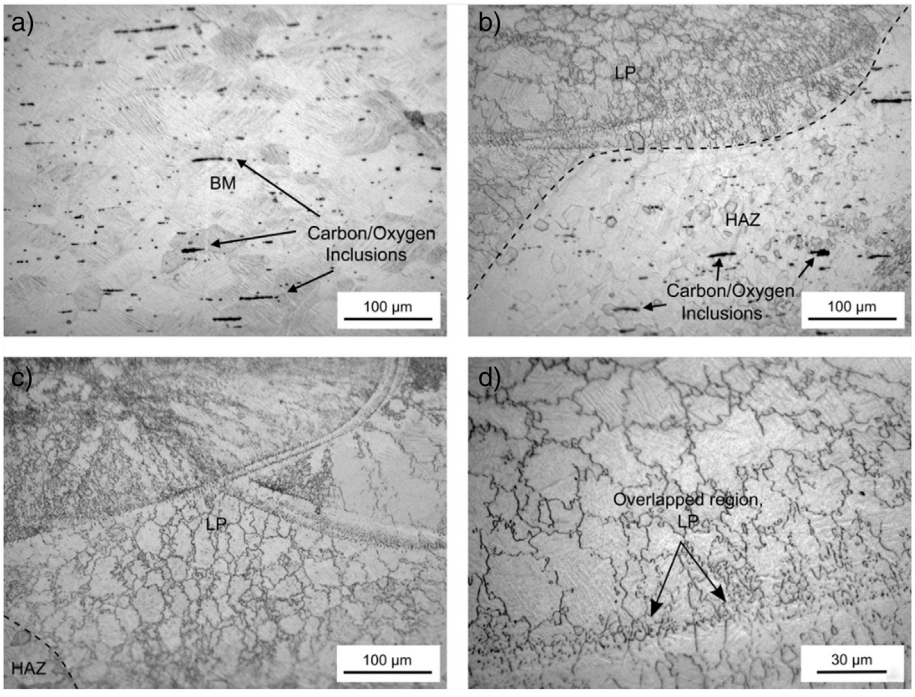


**Fig. 3.** Microstructure of cross-sectioned samples. a) BM (i.e. CE) with larger carbon/oxygen inclusions indicated by arrows, b) LP/HAZ interface with larger carbon/oxygen inclusions in HAZ, as indicated by arrows, c) overlapped laser spots, and d) high magnification image of LP region with boundary between different laser spots indicated by arrows.

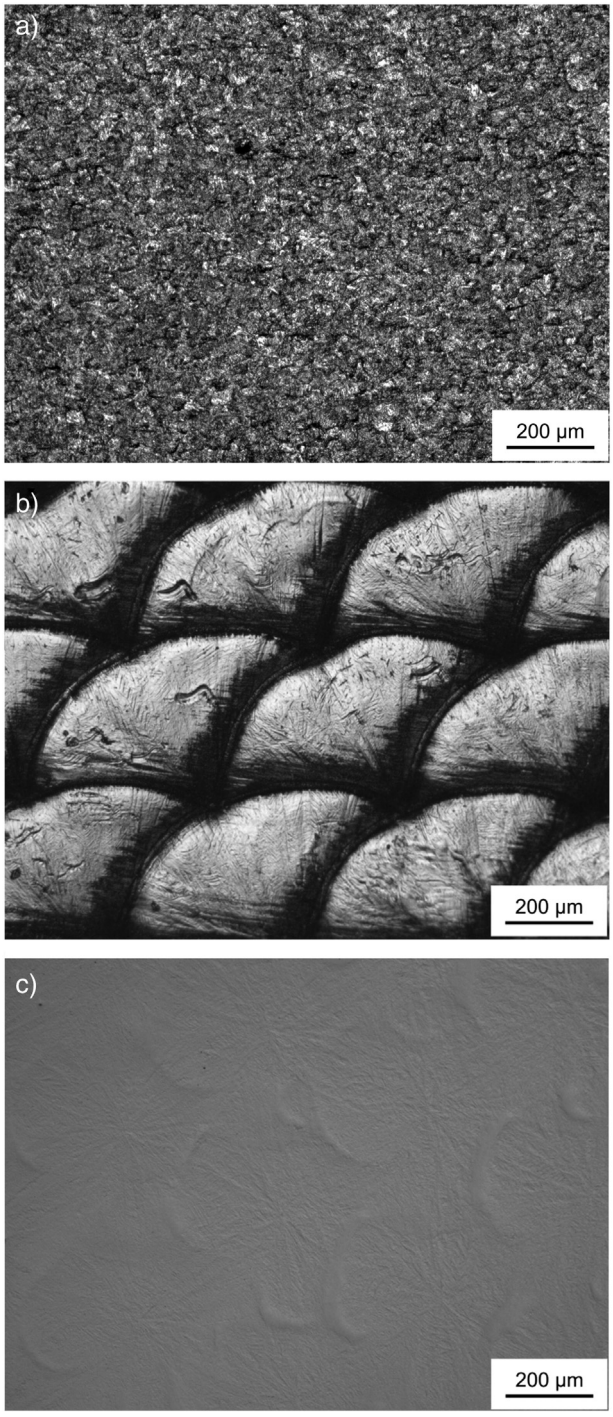


**Fig. 4.** Optical micrographs of a) the NiTi after chemical ecthing, b) laser processing and c) and mechanical polishing (LP-Pol).

in the form of metallic oxide ($TiO_2$) with some carbon bonding or possible metallic hydroxides on the surface.

Surface XPS analysis of the LP sample, shown in Fig. 7, also contained trace amounts of elemental Ni, however $Ni_2O_3$ was also identified. Although at a binding energy of 855.66 eV constituents other than $Ni_2O_3$ are possible, the known presence of a black plume deposited on the surface during laser processing [18] suggests that it was in fact $Ni_2O_3$. Furthermore, the intensity of elemental Ni increased with etching depth; however $Ni_2O_3$ was not detected below the surface. Titanium on the surface also formed an oxide in the form of $TiO_2$, which shifted to metallic Ti deeper into the sample surface. A relatively more gradual change from $TiO_2$ to metallic Ti is indicative of a thicker oxide layer. Oxygen was mostly in the form of metallic oxide ($TiO_2$) with some carbon bonding or possible metallic hydroxides on the surface, similar to the CE sample (Fig. 6).

Analysis of the LP-Pol, shown in Fig. 8, identified a greater amount of elemental Ti and Ni on the surface compared to the CE and LP samples. Titanium was primarily in the form of $TiO_2$ and shifted to metallic Ti as depth increased. A more rapid change from $TiO_2$ to metallic Ti was indicative of a thinner oxide layer compared to both the CE and LP samples. Oxygen was mostly in the form of metallic oxide ($TiO_2$), however some hydrated Ti from polishing was observed; in agreement with previous studies investigating mechanically polished NiTi surfaces [7].

The AES depth profiles of the C, O, Ni and Ti signals for all samples are shown in Fig. 9. These graphs plot relative atomic concentration as a function of $SiO_2$ etch time. For all samples, the oxygen intensity starts out relatively low due to the high amount of carbon contamination on the surface and increases as carbon decreases. This carbon contamination is most likely from storage and transportation of the sample prior to AES analysis. After passing through the oxide layer, the oxygen decreases to the bulk concentration. The oxide thicknesses for the CE and LP samples were 11.5 nm and 13.5 nm, respectively. In contrast, the oxide thickness for the LP-Pol sample was about half that of CE and LP samples, near 6 nm. No significant Ni enrichment of the surface interior was identified in any of the samples. Thick oxides must be present to begin to observe this Ni enriched layer [40]. The oxygen and carbon levels remain quite high in the extreme surface interior/bulk of the CE sample compared to those in the laser processed samples. This could be an artefact of higher contaminant levels (i.e. large TiC and $Ti_2NiO_x$ inclusions) resulting from the material manufacturing process [27].

From the Raman spectrometry results given in Fig. 10, the degree of crystallinity of the surface oxide was identified. It was observed that the CE and LP-Pol samples had an amorphous surface oxide by the absence of measured Raman bands. For the LP sample, an amorphous surface oxide was also identified within a laser spot (LP1 region, Fig. 10b). However, adjacent to where the laser spots overlap, in an approximately 20 μm wide band (LP2 region, Fig. 10b), some degree of crystallinity was observed. The low intensity, broad nature of the measured Raman bands in this LP2 region can result from the thin nature of the oxide layer and/or low degree of crystallinity respectively [41], making definitive crystal structure identification difficult. From past literature it has been shown that $TiO_2$ in either the Rutile and Anatase crystal structures and even $TiNiO_3$ have been identified on the surface of NiTi [41,42]; each of which have Raman bands which may contribute to the trend identified in Fig. 10.

### 3.5. Cyclic potential polarization and Ni ion release

Representative cyclic potential polarization curves for each of the samples are shown in Fig. 11. The breakdown potential of the LP sample was lower than both the CE and LP-Pol samples, as it broke down and corroded at a significantly lower potential (i.e. 522 ± 48 mV vs SCE). Each sample had a similar current density ranging between $7 \times 10^{-7}$ and $7.5 \times 10^{-7}$ A/cm$^2$ in the passive region of the curve, indicating similar rates of metal dissolution. Spikes in the current density were observed in the CE curve, which likely correspond to rapid pitting and repassivation. The corrosion potentials were found to vary by >100 mV for all tests.

Scanning electron micrographs of the NiTi surface following the potendiodynamic cyclic polarization tests are provided in Fig. 12. The CE and LP-Pol samples showed uniform pitting across the surface; shown in Fig. 12a and c. Pit defects observed in the LP-Pol sample were much smaller compared to the CE sample. In the LP sample, only few areas exhibited extensive localized corrosion, as shown in Fig. 12b. It was noted that localized corrosion in the LP samples was preferential where the laser spots overlap each other, as illustrated by

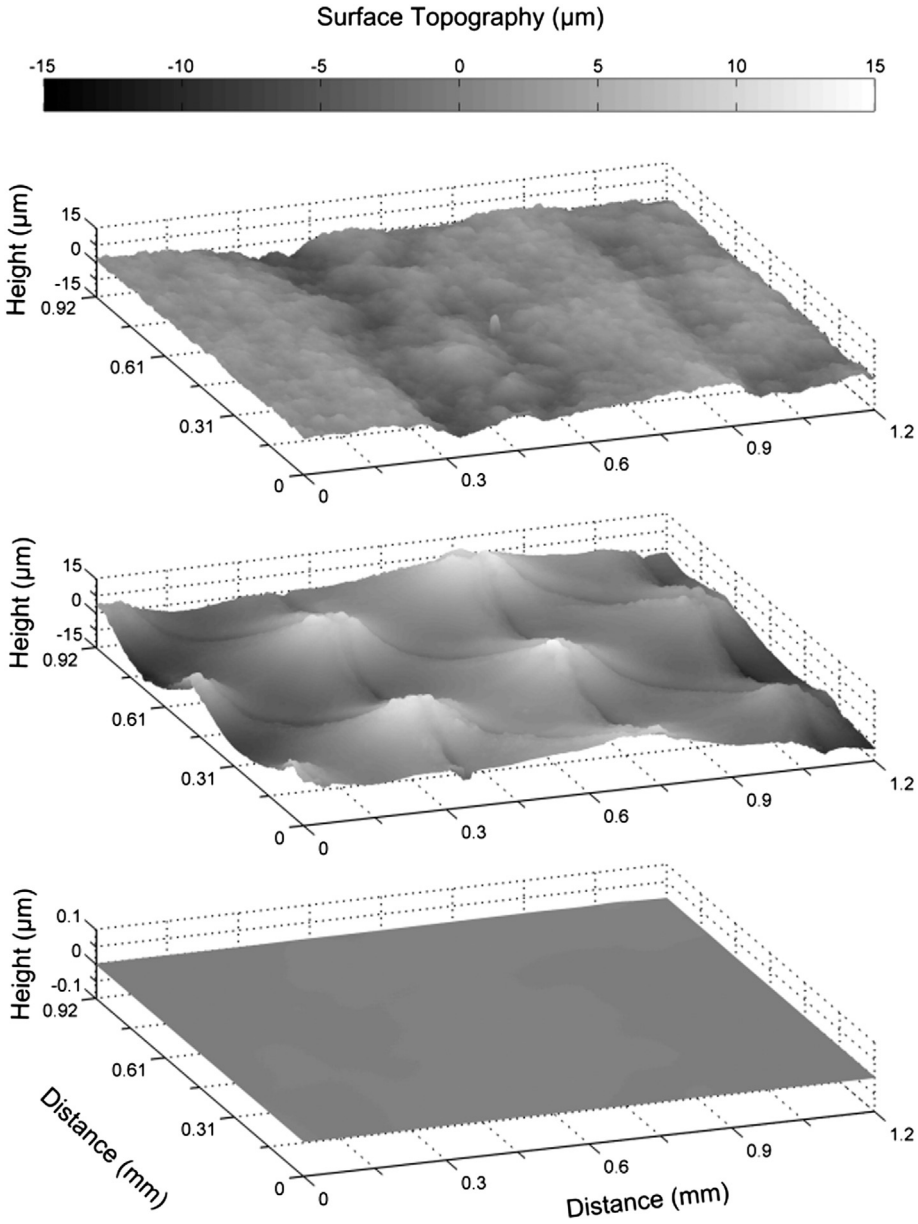


**Fig. 5.** 3D topographical surface maps for a) CE (Ra = 1.63 μm), b) LP (Ra = 2.43 μm) and c) LP-Pol (Ra = 0.01 μm) samples prior to corrosion testing.

the dashed lines in Fig. 12b. Therefore corrosion originated in the LP2 region adjacent to each pulse (Fig. 10b).

The amount of Ni ions released into the PBS solution after 7 days for the CE and LP-Pol samples was below the detection limit of 13.2 μg/L (13.2 ppb). However, Ni ion release for the LP samples was 28.6 μg/L, 12.3 μg/L above the control sample.

## 4. Discussion

### *4.1. Effects of laser processing on surface characteristics*

The corrosion performance and biocompatibility of NiTi SMAs are strongly linked to factors such as chemical composition, oxide thickness, surface chemistry, and roughness [8,20,22,23,28,43]. It is therefore necessary to further discuss the effects of laser processing on these material characteristics.

Chemical composition plays a particularly important role in the formation of chemical species on a material's surface, where amorphous $TiO_2$ is preferred over mixtures of Ni- and Ti-oxides and the presence of elemental Ni is undesirable all together [6,7,44]. Following laser processing the surface and bulk material composition can drastically change [19]. Moreover, in the current work laser processing parameters were selected to induce preferential vaporization of Ni, leaving a Ni depleted region in the bulk material. Although this change in composition was small, evidence of preferential vaporization can be observed in the DSC results shown in Fig. 2, where the Ni depleted LP material exhibited higher phase transformation temperatures. Specifically, the 86.5 °C increase in the $M_s$ transformation temperature (Table 1) can be used to estimate the change in local bulk chemical composition using thermodynamic models [39,45]. A decrease in the Ni composition of 0.48 at.% was predicted using Tang's model (i.e. 180° change/at.% Ni) [45] and an even larger decrease of 1.04 at.% Ni was predicted using the more recent model presented by Frenzel et al. [39] (i.e. 83° change/at.% Ni). An increase in bulk material Ti/Ni ratio following laser processing was suggested by Man et al. [23] to be one of the mechanisms behind improved corrosion performance of laser surface melted NiTi SMAs. A higher bulk

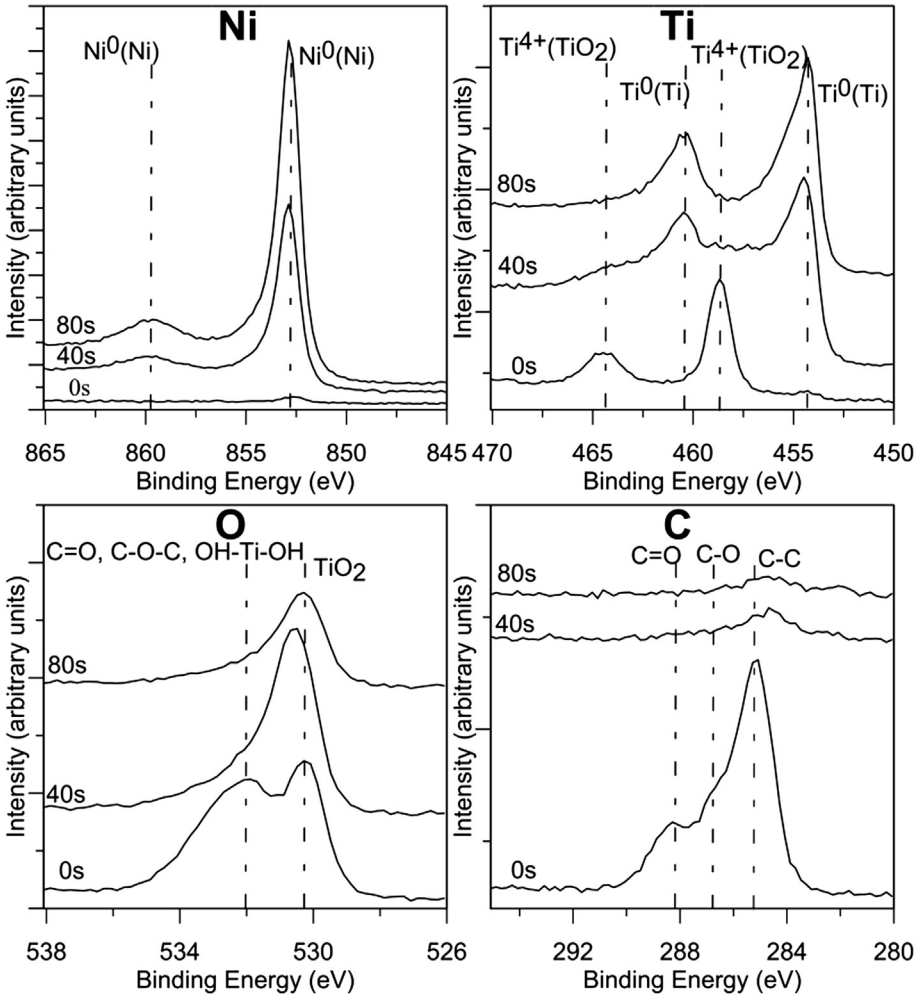


**Fig. 6.** XPS depth profile of the NiTi CE sample prior to corrosion testing at 0 s, 60 s and 80 s etch times.

Ti/Ni ratio was implied to correlate with an improvement of Ti/Ni ratio at the material surface, leading to the formation of a more robust $TiO_2$ oxide.

To investigate this mechanism further and for better comparison with literature [46], the Ti/Ni ratios measured via AES analysis were plotted as a function of depth in Fig. 13. Initially, the Ti/Ni ratios increase with depth because the carbon contamination present on the surface decreases the relative amount of Ti; as carbon decreases the Ti/Ni ratio increases. The source of the carbon contamination is most likely the storage and transportation of the samples prior to Auger analysis. After passing through the oxide layer the Ti/Ni ratio decreases to the bulk concentration. This trend of the Ti/Ni ratio first increase then decreasing was also observed by Trigwell et al., and they even went so far as to use the depth of the maximum Ti/Ni ratio as the oxide thickness of the surface oxide layer [46].

The higher Ti/Ni ratios observed in the CE and LP samples reflect Ni depletion that occurs during the chemical etching and laser processing procedures respectively [19,29,47]. The LP and CE samples had similar Ti/Ni ratios on the surface; however the LP sample did in fact show a slightly higher maximum ratio and the ratio remained higher to a greater depth. This suggests that more Ni was removed from the surface during laser processing compared to chemical etching and correlates well with greater oxide thickness identified on the LP sample (Fig. 9). The LP-Pol sample however, had a much lower Ti/Ni ratio and reached bulk concentrations sooner than both the CE and LP samples.

Now with a better understanding of the composition of the bulk material and the subsurface layers, it is essential to discuss the oxide species that form on each respective substrate as well as other importance surface characteristics, such as surface roughness and degree of crystallinity of oxides. In this study, the CE sample was selected as the baseline since chemical etching was already a necessary step to remove the thick black oxide prior to NiTi medical device deployment, to clean the surface and build $TiO_2$ while leaching out Ni [29,47]. Furthermore this black oxide has also been shown to cause embrittlement of the laser processed region [48]. After etching, the CE samples had a rough pitted appearance with a roughness value, Ra of 1.63 μm (Figs. 4 and 5). The surface chemistry of the CE sample was similar to that found in literature [29] where amorphous $TiO_2$ oxide was found to preferentially form with only trace amounts of elemental Ni present (Figs. 6 and 10).

In contrast to the CE samples, the LP samples were subjected to several high power density laser pulses. However, aside from the presence of $Ni_2O_3$, surface chemistry was similar to the CE sample (Figs. 6 and 7). Since $Ni_2O_3$ was no longer detectable after a 20 s sputter during XPS analysis it was only present on the topmost surface layer and was presumed to result from condensation of Ni-rich plume during laser processing [18]. The LP sample oxide was formed on top of the resolidified material and subjected to several heating cycles as adjacent laser spots were made. These subsequent thermal cycles can contribute to thickening of the oxide. The LP material exhibited only a slightly thicker oxide layer (13.5 nm) than the CE specimen (11.5 nm). The Ar shielding used in the laser process prevented excessive oxide growth by limiting the oxygen available for reaction. Thermal cycles experienced during processing in the LP samples however, may have resulted

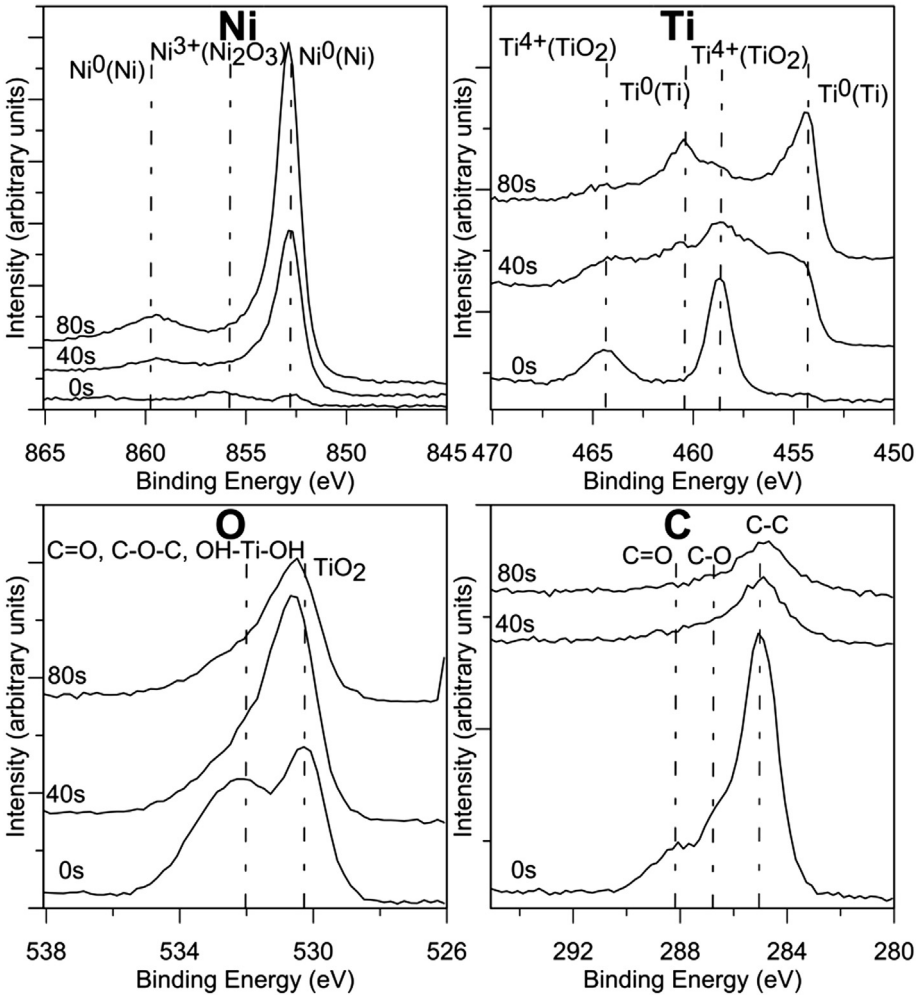


**Fig. 7.** XPS depth profile of the NiTi LP sample prior to corrosion testing at 0 s, 60 s and 80 s etch times.

in the ~20 μm wide LP2 region, having a higher degree of crystallization, adjacent to each laser spot as shown in Fig. 10.

The LP-Pol sample showed higher amounts of elemental Ti and Ni on the surface compared to the LP and CE samples (Fig. 8). The increase in elemental Ti was due to only partial oxidation of Ti in air at room temperature [7]. Partial oxidation also contributed to the lowest Ti/Ni ratio, shown in Fig. 13, while forming the thinnest oxide layer of 6 nm. This higher elemental Ni concentration can be attributed to mechanical polishing procedure not selectively removing Ni, while acid etching and laser processing do so through leaching [29,47] and vaporization [19] mechanisms respectively. Mechanical polishing did, however, decrease the surface roughness to a Ra value of 0.01 μm from a Ra value of 2.43 μm (Fig. 5) and facilitated the formation of a favourable uniform, amorphous oxide on the surface (Fig. 10).

### 4.2. Corrosion and Ni ion release performance

It has previously been shown that chemical etching produces a surface that is highly resistant to both general and pitting corrosion [30,47]. The CE sample tested in this study showed the best corrosion resistance through cyclic polarization testing. When considering only the increase in Ti/Ni ratio and oxide thickness, the LP sample could be expected to have a similar performance as the CE sample. Moreover, according to literature, laser surface melting can improve corrosion performance [23, 28]. However, the LP samples exhibited a breakdown potential of about half that of the CE and LP-Pol samples (i.e. 522 ± 48 mV vs SCE) as well as exhibiting the highest Ni ion release of 28.6 μg/L.

There are several factors that contribute to the decreased breakdown potential and increase in Ni ions released from the LP sample. The re-melted surface of the laser spot was relatively smooth compared to the roughness values of the CE material, which has been suggested in several studies [22,23,27,28] to contribute to an improved corrosion behaviour of laser processed NiTi. However, micro-crevices also formed at the intercept of four laser spots (Fig. 5) along with a region of higher crystallinity adjacent to each laser spot (Fig. 10). This topography leads to the highest overall roughness measured of all three samples. Since localized corrosion was observed to occur where the laser spots intercept (Fig. 12b), micro-crevices and partially crystalline oxide in the LP2 region were concluded to play a critical role in degrading corrosion performance. Another possible contribution to decrease corrosion resistance and increased Ni ions released was the presence of $Ni_2O_3$ on the top surface of the LP samples. Previous studies have shown that a homogeneous oxide is more stable than a heterogeneous oxide [7]. A mixture of oxides can lead to a segregation of species that leaves the oxide layer more susceptible to corrosion. In addition, an amorphous oxide layer is also more stable and corrosion resistant [7].

As mentioned above, a higher Ti/Ni ratio suggests the formation of a more robust protective oxide layer however, in the bulk material this can also lead to the formation of secondary phases between dendrites due to microsegregation. In laser surface melting Man et al. [23] and Cui et al. [28] both imply Ni constituent loss due to vaporization and

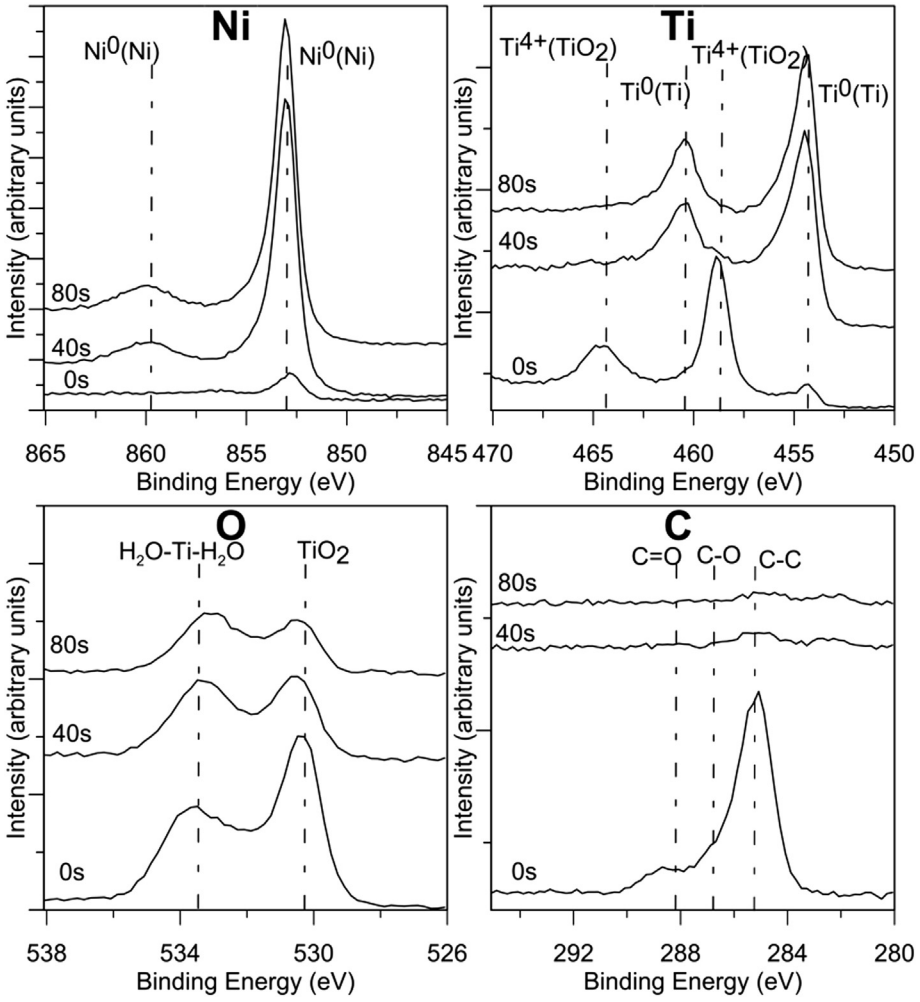


**Fig. 8.** XPS depth profile of the NiTi LP-Pol sample prior to corrosion testing at 0 s, 60 s and 80 s etch times.

they identified the $Ti_2Ni$, Ti-rich phase using X-ray diffraction in the laser melted region. Secondary phases, $Ti_2Ni$ and $Ti_2NiO_x$ were also identified at prior parent grain boundaries due to microsegregation and oxygen pick-up in a previous study utilizing a pulsed laser induced vaporization protocol [19]. The secondary phases identified in the LP cross-sectioned sample (Fig. 3) were therefore, likely also $Ti_2Ni$ or $Ti_2NiO_x$. The presence of inclusions on the surface of NiTi also affects the homogeneity/uniformity and therefore stability of the oxide layer [6]. Also, Ni-rich regions form around Ti-rich phases leading to the presence of elemental Ni and increased Ni ion release [6].

**Table 2**
Species identified via XPS analysis on the CE, LP and LP-Pol surfaces and their respective binding energies (eV).

| | Peak energy (eV) | Constituent | Present in sample | | |
|---|---|---|---|---|---|
| | | | CE | LP | LP-Pol |
| Ni | 852.68 | Ni $2p^{2/3}$ | Yes | Yes | Yes |
| | 855.66 | $Ni_2O_3$ | No | Yes | No |
| | 859.51 | sat. Ni $2p^{2/3}$ | Yes | Yes | Yes |
| Ti | 454.85 | Ti $2p^{2/3}$ | Yes | Yes | Yes |
| | 458.76 | $TiO_2$ $2p^{2/3}$ | Yes | Yes | Yes |
| | 460.48 | Ti $2p^{2/3}$ | Yes | Yes | Yes |
| | 464.40 | $TiO_2$ $2p^{2/3}$ | Yes | Yes | Yes |
| Oxygen | 530.24 | $TiO_2$ | Yes | Yes | Yes |
| | 532.40 | C═O, C–O, OH–Ti–OH | Yes | Yes | No |
| | 533.76 | $H_2O$–Ti–$H_2O$ | No | No | Yes |
| Carbon | 285.17 | C–C | Yes | Yes | Yes |
| | 286.63 | C–O | Yes | Yes | Yes |
| | 288.32 | C═O | Yes | Yes | Yes |

After mechanical polishing, the LP-Pol sample had comparable corrosion resistance as the CE sample. Similar results were also observed from the Ni ion release test where both the CE and LP-Pol samples produced no detectable amount of Ni ions after a 7 day immersion in PBS solution. Mechanical polishing of the laser processed material removes any undesirable surface topography, crystallized oxides, and $Ni_2O_3$ species. The thin amorphous oxide with lower Ti/Ni ratio (Figs. 9 and 13) was found to have improved corrosion and Ni ion release performance. These results suggest that changes to the bulk material from laser processing such as, increased Ti/Ni ratio and the formation of $Ti_2Ni$ and $Ti_2NiO_x$ phases at dendritic grain boundaries did not significantly affect the corrosion resistance of the bulk material. The change in corrosion resistance observed in the LP material comes from one or more characteristics present on the topmost surface, which can be removed via post-processing procedures such as mechanical polishing.

### 4.3. Laser processed NiTi as a biomaterial

Just as in other NiTi processing techniques, the corrosion and biocompatibility of laser processed NiTi surfaces can vary depending on many factors. The current work showed, contrary to other laser processing studies examining laser surface melting [23,28] or laser welding [21, 22,25,26], that the corrosion performance and Ni ion release levels were

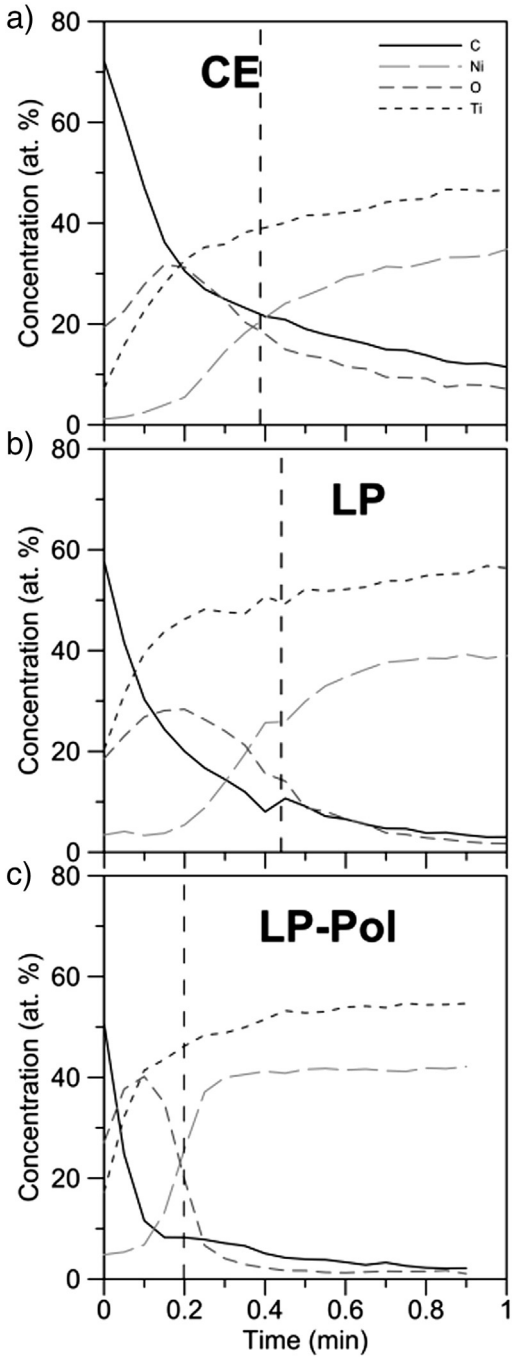


**Fig. 9.** Auger depth profiles for a) CE, b) LP, and c) LP-Pol samples prior to corrosion testing. The vertical dashed line corresponds to the approximated oxide thickness.

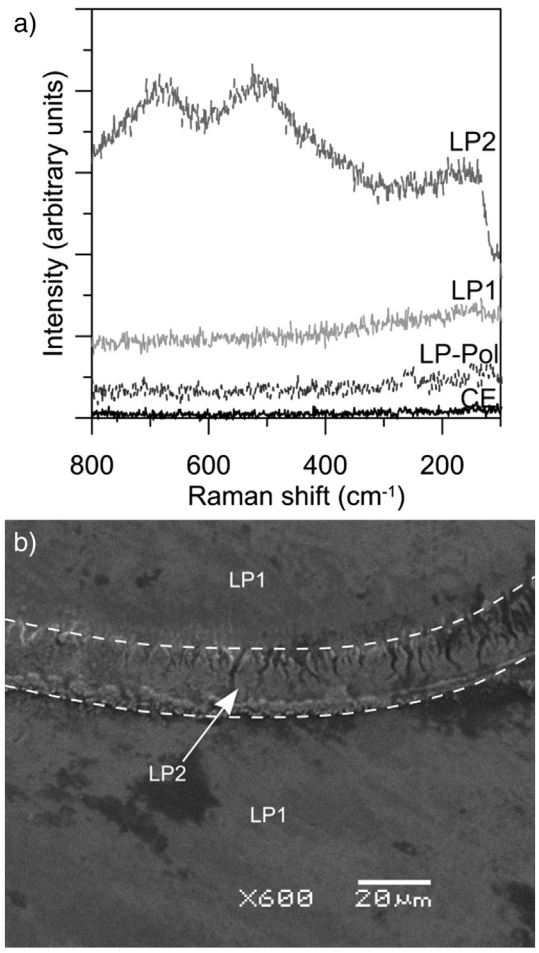


**Fig. 10.** a) Raman spectra the CE, LP, and LP-Pol samples prior to corrosion testing. b) SEM scanning electron images at 20 kV of the LP2 region where adjacent laser spots overlap (located between the dashed lines).

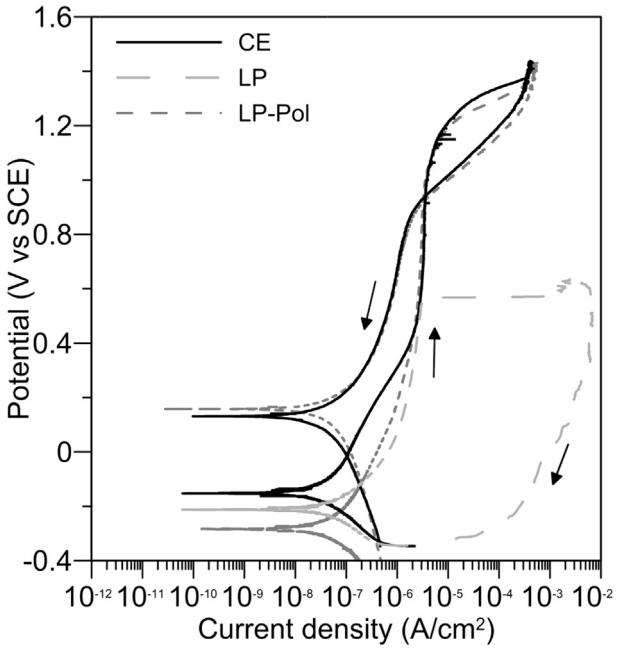


**Fig. 11.** Representative potentiodynamic cyclic polarization curves for CE, LP and LP-Pol samples. Potentiodynamic cyclic polarization tests were performed in a phosphate buffer saline (PBS) electrolyte (pH 7.4) at 37 °C with a scan rate of 0.167 mV/s using a saturated calomel electrode (SCE) as the reference electrode and a Pt mesh as the counter electrode.

not improve immediately after processing; in line with the findings of Chan et al. [9].

Even though a decrease in breakdown potential was observed in the current study, the magnitude was still on par with stainless steel [4] and the metal dissolution rate remained unchanged in the passive region. Moreover, based on the number of days tested and volume of PBS solution used in the Ni ion release test, the average Ni ion release rate of as-laser processed material (LP) was negligible compared to the daily dietary intake of 300–500 μg/day [49], the critical concentration for allergic response of 600–2500 μg/day [50], and the in vitro cytotoxicity limit of 30 ppm [51]. So taken in context, although the corrosion and ion release performance of the LP sample were worse compared to the other sample conditions analysed in this study, the performance in general was

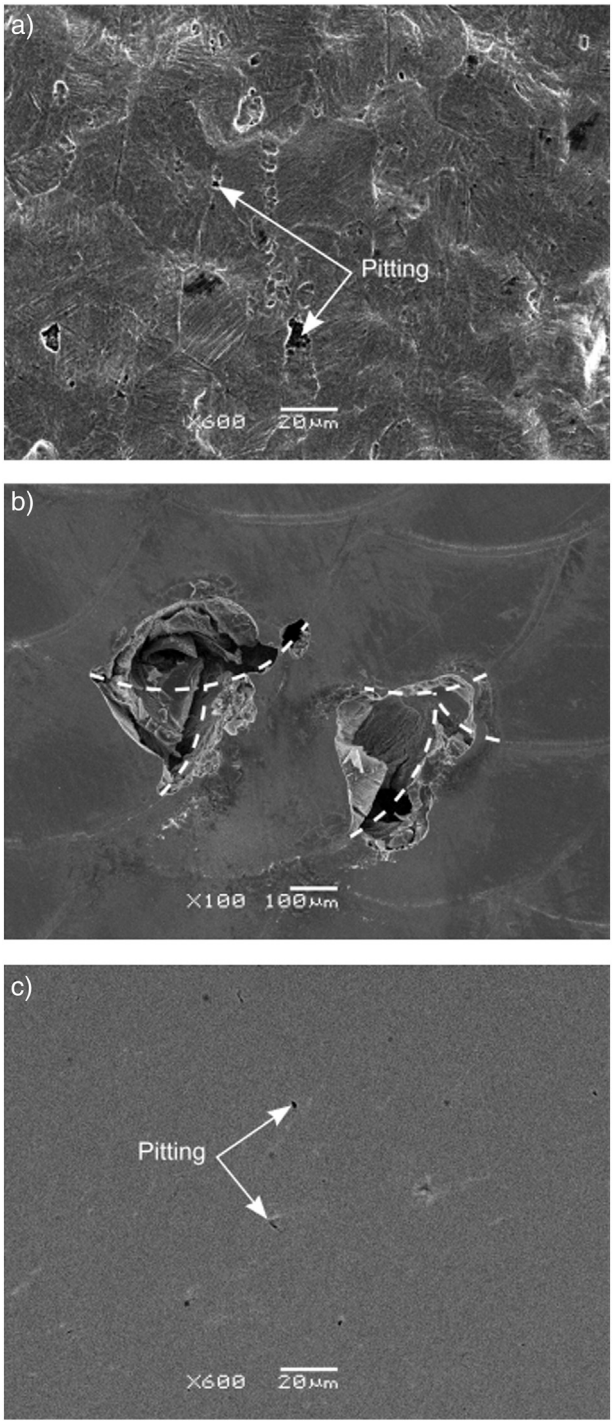


**Fig. 12.** SEM scanning electron images at 20 kV of corroded surfaces: a) CE; b) LP; and c) LP-Pol. Corrode surfaces are taken after potentiodynamic cyclic polarization testing in a phosphate buffer saline (PBS) electrolyte (pH 7.4) at 37 °C with a scan rate of 0.167 mV/s using a saturated calomel electrode (SCE) as the reference electrode and a Pt mesh as the counter electrode.

still good. For example in less demanding medical applications such as minimally invasive surgical tools, which have relatively short service lives and limited exposure to patients, the performance of as-laser processed materials could be acceptable. Moreover, it was shown that for more demanding biocompatibility applications such as, implantable medical devices, laser processed NiTi SMAs can also be used as long as the effects of processing on the surface characteristics are well understood and if necessary, an appropriate post-laser-process surface treatment is utilized.

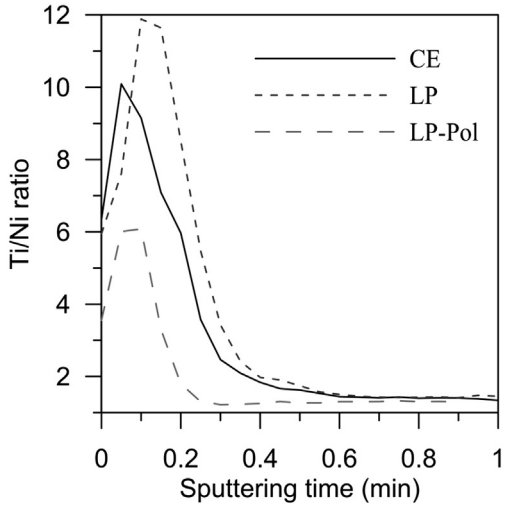


**Fig. 13.** Ti/Ni ratio depth profiles measured via AES for the CE, LP and LP-Pol samples prior to corrosion testing.

## 5. Conclusions

The current study systematically investigated the corrosion performance and Ni ion release performance of a laser processed NiTi. Surface conditions, including chemistry, oxide thickness, composition, microstructure, and roughness, were thoroughly characterized. The most significant findings of this study included:

1. Laser processing removed large TiC, $Ti_2Ni$, and $Ti_2NiO_x$ inclusions present in the base material. Fine secondary phases, likely $Ti_2Ni$ and $Ti_2NiO_x$, were identified at dendritic grain boundaries in the solidification structure. The LP-Pol samples displayed excellent corrosion resistance and non-detectable levels of Ni-ion release, therefore these secondary phases did not significantly reduce the corrosion performance of the bulk material.
2. Superficial surface conditions such as an undesirable surface topography, the existence of a crystalline oxide region in the HAZ, and the presence of $Ni_2O_3$ oxide resulting from plume deposits on the surface led to localized corrosion of the LP samples and a higher cumulative amount of Ni-ion release. Following mechanical polishing of the LP material the corrosion performance and Ni ion release performance were restored.
3. A decrease in bulk material Ni composition on the order of 0.48–1.04 at.% following laser processing had insignificant effects on corrosion performance and Ni ion release compared to surface characteristics induced by the pulsed laser process. Therefore, minor changes in to the bulk concentration of Ni do not affect the performance of the surface oxide.
4. The corrosion resistance and amount of Ni ion release after pulsing with an Nd:YAG laser remained acceptable for the NiTi SMA. However, with appropriate post-processing treatments, such as mechanical polishing, the performance can be greatly improved, allowing for their utilization in a wider range of medical applications including the demanding biocompatibility requirements of implantable devices.

## Acknowledgements

The authors would like to acknowledge the financial support of the Natural Sciences and Engineering Research Council of Canada (NSERC, www.nserc.ca), the Canadian Research Chairs Program (CRC, www.chairs-chaires.gc.ca), and the Ontario Centres of Excellence (OCE, www.OCE-ontario.org). The expertise and technical support of Surface Interface Ontario (www.si-ontario.utoronto.ca), Surface Science Western (www.surfacesciencewestern.com), Smarter Alloys Inc. (smarteralloys.com),

and the Microwelding group of the Centre for Advanced Materials Joining (CAMJ, mme.uwaterloo.ca/~camj/) were also essential to the completion of this study.

## References


[1] J.M. Jani, M. Leary, A. Subic, M.A. Gibson, A review of shape memory alloy research, applications and opportunities, Mater. Des. 65 (2014) 1078–1113.
[2] T. Duerig, A. Pelton, D. Stöckel, An overview of Nitinol medical device applications, Mater. Sci. Eng. A 273–275 (1999) 149–160.
[3] T.G. Frank, W. Xu, A. Cuschieri, Instruments based on shape-memory alloy properties for minimal access surgery, interventional radiology and flexible endoscopy, Minim. Invasive Ther. Allied Technol. 9 (2000) 89–98.
[4] D.J. Wever, A.G. Veldhuizen, J. de Vries, H.J. Busscher, D.R.A. Uges, J.R. van Horn, Electrochemical and surface characterization of a nickel–titanium alloy, Biomaterials 19 (1998) 761–769.
[5] S.A. Shabalovskaya, Surface, corrosion and biocompatibility aspects of nitinol as an implant material, Biomed. Mater. Eng. 12 (2002) 69–109.
[6] S. Shabalovskaya, J. Anderegg, J. van Humbeeck, Critical overview of Nitinol surfaces and their modifications for medical applications, Acta Biomater. 4 (2008) 447–467.
[7] S.A. Shabalovskaya, J. Anderegg, G. Rondelli, W. Vanderlinden, S. De Feyter, Comparative in vitro performances of bare Nitinol surfaces, Biomed. Mater. Eng. 18 (2008) 1–14.
[8] O. Cissé, O. Savadogo, M. Wu, L'H. Yahia, Effect of surface treatment of NiTi alloy on its corrosion behavior in Hanks' solution, J. Biomed. Mater. Res. A 61 (2002) 339–345.
[9] C.W. Chan, H.C. Man, T.M. Yue, Effect of post-weld heat-treatment on the oxide film and corrosion behaviour of laser-welded shape memory NiTi wires, Corros. Sci. 56 (2012) 158–167.
[10] C.W. Chan, H.C. Man, T.M. Yue, Susceptibility to stress corrosion cracking of NiTi laser weldment in Hanks' solution, Corros. Sci. 57 (2012) 260–269.
[11] G. Rondelli, B. Vincentini, A. Cigada, The corrosion behaviour of nickel titanium shape memory alloys, Corros. Sci. 30 (1990) 805–812.
[12] J.K. Bass, H. Fine, G.J. Cisnero, Nickel hypersensitivity in the prosthodontics patient, Am. J. Orthod. Dentofac. Orthop. 103 (1993) 280–285.
[13] M. Berger-Gorbet, B. Broxup, C. Rivard, L'H. Yahia, Biocompatibility testing of Ni–Ti screw using immune histochemistry on section containing metallic implants, J. Biomed. Mater. Res. A 32 (1996) 243–248.
[14] M.I. Khan, Y.N. Zhou, Innovative Processing Technologies, assignee. Methods and Systems for Processing Materials, Including Shape Memory Materials. World Patent application WO/2011/014962, 2010.
[15] M. Daly, A. Pequegnat, Y. Zhou, M.I. Khan, Enhanced thermomechanical functionality of a laser processed hybrid NiTi–NiTiCu shape memory alloy, Smart Mater. Struct. 21 (2012) 045028.
[16] M. Daly, A. Pequegnat, Y. Zhou, M.I. Khan, Fabrication of a novel laser-processed NiTi shape memory microgripper with enhanced thermomechanical functionality, Intell. Mater. Syst. Struct. 24 (2013) 984–990.
[17] A. Pequegnat, M. Daly, J. Wang, Y. Zhou, M.I. Khan, Dynamic actuation of a novel laser processed NiTi linear actuator, Smart Mater. Struct. 21 (2012) 094004.
[18] M.I. Khan, A. Pequegnat, Y. Zhou, Multiple memory shape memory alloys, Adv. Eng. Mater. 15 (2013) 386–393.
[19] A. Pequegnat, Y. Zhou, Microstructure and unique functional properties of laser processed NiTi multiple memory shape memory alloys, Acta Metall. (2015) (submitted for publication).
[20] Q. Meng, Y. Liu, H. Yang, B.S. Shariat, T.H. Nam, Functionally graded NiTi strips prepared by laser surface anneal, Acta Mater. 60 (2012) 1658–1668.
[21] X.J. Yan, D.Z. Yang, X.P. Liu, Electrochemical behavior of YAG laser-welded NiTi shape memory alloy, Trans. Nonferrous Metals Soc. China 16 (2006) 572–576.
[22] X.J. Yan, D.Z. Yang, Corrosion resistance of laser spot-welded joint of NiTi wire in simulated human body fluids, J. Biomed. Mater. Res. A 77 (2006) 97–102.
[23] H.C. Man, Z.D. Cui, T.M. Yue, Corrosion properties of laser surface melted NiTi shape memory alloy, Scr. Mater. 45 (2001) 1447–1453.
[24] P. Sevilla, F. Martorell, C. Libenson, J.A. Planell, F.L. Gil, Laser welding of NiTi orthodontic archwires for selective force application, J. Mater. Sci. Mater. Med. 19 (2008) 525–529.
[25] Y.T. Hsu, Y.R. Wang, S.K. Wu, C. Chen, Effect of $CO_2$ laser welding on the shape memory and corrosion characteristics of TiNi alloys, Metall. Mater. Trans. A 32 (2001) 569–576.
[26] F. Villermaux, M. Tabrizian, L'H. Yahia, M. Meunier, D.L. Piron, Excimer laser treatment of NiTi shape memory alloy biomaterials, Appl. Surf. Sci. 109–110 (1997) 62–66.
[27] X.J. Yan, D.Z. Yang, X.P. Liu, Corrosion behavior of a laser-welded NiTi shape memory alloy, Mater. Charact. 58 (2007) 623–628.
[28] Z.D. Cui, H.C. Man, X.J. Yang, The corrosion and nickel release behavior of laser surface-melted NiTi shape memory alloy in Hanks, solution, Surf. Coat. Technol. 192 (2005) 347–353.
[29] S. Shabalovskaya, J. Anderegg, F. Laab, P.A. Thiel, G. Rondelli, Surface conditions of Nitinol wires, tubing, and as-cast alloys: the effect of chemical etching, aging in boiling water, and heat treatment, J. Biomed. Mater. Res. A Appl. Biomater. 65 (2003) 193–203.
[30] N. Munroe, C. Pulletikurthi, W. Haider, Enhanced biocompatibility of porous Nitinol, J. Mater. Eng. Perform. 18 (2009) 765–767.
[31] W. Haider, N. Munroe, Assessment of corrosion resistance and metal ion leaching of nitinol alloys, J. Mater. Eng. Perform. 20 (2011) 812–815.
[32] C. Liu, P.K. Chu, G. Lin, D. Yang, Effects of Ti/TiN multilayer on corrosion resistance of nickel–titanium orthodontic brackets in artificial saliva, Corros. Sci. 49 (2007) 3783–3796.
[33] B.G. Pound, Susceptibility of nitinol to localized corrosion, J. Biomed. Mater. Res. A 77 (2006) 185–191.
[34] Z. Huan, L.E. Fratila-Apachitei, I. Apachitei, J. Duszczyk, Effect of aging treatment on the in vitro nickel release from porous oxide layers on NiTi, Appl. Surf. Sci. 274 (2013) 266–272.
[35] Y. Okazaki, E. Gotoh, Metal release from stainless steel, Co–Cr–Mo–Ni–Fe and Ni–Ti alloys in vascular implants, Corros. Sci. 50 (2008) 3429–3438.
[36] D. Vojtech, J. Kubasek, M. Voderova, P. Seda, A. Michalcova, Study of mechanical, fatigue and corrosion, properties of the superelastic Ni–Ti alloy, Proceedings of 20th Anniversary International Conference on Metallurgy Materials, Czech Republic, EU, 2011, pp. 1–7.
[37] A. Michiardi, C. Aparicio, J.A. Planell, F.J. Gil, New oxidation treatment of NiTi shape memory alloys to obtain Ni-free surfaces and to improve biocompatibility, J. Biomed. Mater. Res. A Appl. Biomater. 77 (2006) 249–256.
[38] G. Fan, W. Chen, S. Yang, J. Zhu, X. Ren, K. Otsuka, Origin of abnormal multi-stage martensitic transformation behavior in aged Ni-rich Ti–Ni shape memory alloys, Acta Mater. 52 (2004) 4351–4362.
[39] J. Frenzel, E.P. George, A. Dlouhy, C.H. Somsen, M.F.-X. Wagner, G. Eggeler, Influence of Ni on martensitic phase transformation in NiTi shape memory alloys, Acta Mater. 58 (2010) 3444–3458.
[40] L. Zhu, J.M. Fino, A.R. Pelton, Oxidation of Nitinol, Proceedings of Smart Materials and Superelastic Technologies, California, USA, 2003.
[41] C.L. Chu, C.Y. Chung, P.K. Chu, Surface oxidation of NiTi shape memory alloy in a boiling aqueous solution containing hydrogen peroxide, Mater. Sci. Eng. A 417 (2006) 104–109.
[42] G.S. Firstov, R.G. Vitchev, H. Kumar, B. Blanpain, J. van Humbeeck, Surface oxidation of NiTi shape memory alloy, Biomaterials 23 (2002) 4863–4871.
[43] C.M. Chan, S. Trigwell, T. Duerig, Oxidation of an NiTi alloy, Surf. Interface Anal. 15 (1990) 349–354.
[44] S.A. Shabalovskaya, Physicochemical and biological aspects of nitinol as a biomaterial, Int. Mater. Rev. 46 (2001) 233–250.
[45] W. Tang, Thermodynamic study of the low-temperature phase B19′ and the martensitic transformation in near-equiatomic Ti–Ni shape memory alloys, Metall. Mater. Trans. A 28 (1997) 537–544.
[46] S. Trigwell, R.D. Hayden, K.F. Nelson, G. Selvaduray, Effects of surface treatment on the surface chemistry of NiTi alloy for biomedical applications, Surf. Interface Anal. 26 (1998) 483–489.
[47] S.A. Shabalovskaya, G.C. Rondelli, A.L. Undisz, J.W. Anderegg, T.D. Burleigh, M.E. Rettermayr, The electrochemical characteristics of native Nitinol surfaces, Biomaterials 30 (2009) 3662–3671.
[48] B. Tam, M.I. Khan, Y. Zhou, Mechanical and functional properties of laser-welded Ti-55.8 wt pct Ni Nitinol wires, Metall. Mater. Trans. A 42 (2011) 2166–2175.
[49] H.A. Schroeder, J.J. Balassa, I.H. Tipton, Abnormal trace metals in man — nickel, J. Chronic Dis. 15 (1962) 51–65.
[50] K. Kaaber, N.K. Veien, J.C. Tjell, Low nickel diet in the treatment of patients with chronic nickel dermatitis, Br. J. Dermatol. 98 (1978) 197–201.
[51] H. Bour, J.F. Nicolas, J.L. Garrigue, A. Demiden, D. Schmitt, Establishment of nickel-specific T cells from patients with allergic contact dermatitis: comparison of different protocols, Clin. Immunol. Immunopathol. 73 (1994) 142–145.